Structural and Multidisciplinary Optimization (2023) 66:16
https://doi.org/10.1007/s00158-022-03432-5

RESEARCH PAPER

A reinforcement learning hyper-heuristic in multi-objective optimization with application to structural damage identification

Pei Cao[1] · **Yang Zhang**[1] · **Kai Zhou**[2] · **J. Tang**[1]

Received: 17 June 2022 / Accepted: 14 October 2022 / Published online: 28 December 2022

Abstract
Multi-objective optimization allows satisfying multiple decision criteria concurrently, and generally yields multiple solutions. It has the potential to be applied to structural damage identification applications which are oftentimes under-determined. How to achieve high-quality solutions in terms of accuracy, diversity, and completeness is a challenging research subject. The solution techniques and parametric selections are believed to be problem specific. In this research, we formulate a reinforcement learning hyper-heuristic scheme to work coherently with the single-point search algorithm MOSA/R (Multi-Objective Simulated Annealing Algorithm based on Re-seed). The four low-level heuristics proposed can meet various optimization requirements adaptively and autonomously using the domination amount, crowding distance, and hypervolume calculations. The new approach exhibits improved and more robust performance than AMOSA, NSGA-II, and MOEA/D when applied to benchmark test cases. It is then applied to an active damage interrogation scheme for structural damage identification where solution diversity/completeness and accuracy are critically important. Results show that this approach can successfully include the true damage scenario in the solution set identified. The outcome of this research can potentially be extended to a variety of applications.

Keywords Multi-objective optimization · Hyper-heuristic · Reinforcement learning · Simulated annealing · Structural damage identification

1 Introduction

Many engineering optimization problems involve multiple types of goals, thus naturally present themselves as multi-objective problems. For example, the rapid advancement of sensing and measurement technologies has made it possible to realize structural damage identification in the near real time. Fault parameters in a structure are identified through matching measurements with model predictions in the parametric space. A well-known issue in direct inversion-based techniques in structural damage identification is that the problems formulated are oftentimes under-determined, as the number of measurements is generally smaller than the number of fault parameters (i.e., location and severity of damage) to be identified. Since multiple criteria may be involved in matching measurements with predictions, the identification can be cast into a multi-objective optimization problem. A multi-objective optimization formulation has the potential of overcoming the computational issue in direct inversion.

From a methodology standpoint, multi-objective optimization algorithms have been applied to a variety of applications, ranging from production scheduling (Wang et al. 2014; Lu et al. 2016), structural optimization (Kaveh and Laknejadi 2013; Ye et al. 2017, 2019; Zavala et al. 2014 and 2016; Zarchi and Attaran 2019), performance improvement (Szőllős et al. 2009), to structural damage identification

Responsible Editor: Zhen Hu

Topical Collection: Advanced Optimization Enabling Digital Twin Technology.
Guest Editors: C. Hu, V. A. González, T. Kim, O. San, Z. Hu, and P. Zheng.

✉ J. Tang
jiong.tang@uconn.edu

[1] Department of Mechanical Engineering, University of Connecticut, 191 Auditorium Road, Unit 3139, Storrs, CT 06269, USA

[2] Department of Mechanical Engineering-Engineering Mechanics, Michigan Technological University, Houghton, USA

(Cha and Buyukozturk 2015; Cao et al. 2018a, b; Tiachacht et al. 2018; Gomes et al. 2018; Dinh-Cong and Nguyen-Thoi 2021). However, the solution techniques are often devised and evaluated for specific problem domains, requiring an in-depth understanding of the problem domain involved and challenging to be exercised in different instances. Even for the same type of problems, the formulation may need to be adjusted as more knowledge and insights are gained. One possible approach to tackle this difficulty is the hyper-heuristic concept (Cowling et al. 2000). The terminology implies that a high-level scheme to select heuristic operators is incorporated as the detailed algorithms are executed (Burke et al. 2009), given a particular problem and several low-level heuristics. Instead of finding reasonable solutions, hyper-heuristic is more interested in adaptively finding proper solution methods. Many hyper-heuristic studies have been conducted for multi-objective problems, including problems on benchmarks (Maashi et al. 2015; Zhang et al. 2020) and real-world applications (Guizzo et al. 2015; Hitomi and Selva 2015 2016; Qin et al. 2021). For more discussions about hyper-heuristic techniques, one can refer to literature (Burke et al. 2013).

A hyper-heuristic framework typically involves (1) a high-level strategy to iteratively select among low-level heuristics based on the performance; (2) a predefined repository of low-level heuristics; and (3) applying the heuristics selected into optimization and evaluating their performance. The selection mechanism in hyper-heuristics, which ensures objectivity, specifies the heuristic to apply to a given optimization point without using any domain information. Online learning hyper-heuristics usually take advantage of the concept of reinforcement learning for selection (Ozcan et al. 2012), as they aim to iteratively solve the heuristics selection task by weight adaptation through interactions with the search domain. The low-level heuristics correspond to a set of exploration rules, and each carries a utility value. The values are updated at each step based on the success of the chosen heuristic. An improving move is rewarded, while a worsening move is punished. The low-level heuristics can be embedded in single-point search techniques suited for these tasks because only one neighbor is analyzed for a choice decision (Nareyek 2003). In a single-point search-based hyper-heuristic framework, e.g., simulated annealing (Kirkpatrick et al. 1983)-based hyper-heuristic, an initial candidate solution goes through a set of successive stages repeatedly until termination.

A multi-objective optimization problem inherently features multiple solutions. A major challenge in solving such a problem is finding these multiple solutions in a diverse and complete sense. Incomplete solutions congregated together cannot fully reflect the advantage of multi-objective optimization formulation and may not even satisfy the requirement of the specific engineering problem. To tackle this issue, in this research, we establish a general-purpose framework that incorporates hyper-heuristic systematically into the state-of-the-art Multi-Objective Simulated Annealing (MOSA) approach to improve both the generality and solution performance. We develop a reinforcement learning hyper-heuristic inspired by probability matching (Goldberg 1990), consisting of selection and credit assignment strategies. Recent investigations have shown that the solution quality/diversity and the robustness of MOSA may be enhanced with re-seed schemes (Cao et al. 2019). The re-seed schemes, on the other hand, need to be tailored to fit specific problem formulations. Here, in this research, the re-seed schemes are treated as low-level heuristics, empowering the algorithm to cover various scenarios. The performance and generality of the proposed approach are first demonstrated over commonly recognized benchmark testing cases DTLZ (Deb et al. 2002a b) and UF (Zhang et al. 2008) in comparison with the popular multi-objective algorithms, NSGA-II (Deb et al. 2002a b), AMOSA (Bandyopadhyay et al. 2008), and MOEA/D (Zhang and Li 2007).

This new framework is then applied to the inverse analysis of structural damage identification utilizing piezoelectric-based active interrogation. In such an approach, frequency-sweeping voltage excitation is supplied to a piezoelectric transducer attached to the host structure. Owing to the two-way electro-mechanical coupling, the structural impedance is coupled with the piezoelectric impedance that can be measured based on frequency-sweeping excitation. The measured changes of piezoelectric impedance, in conjunction with the finite element model of the baseline healthy structure, can then be used as damage signatures to facilitate the identification of damage location and severity. In structural health monitoring, one main challenge is to detect/identify small-sized damage at the early stage of damage progression. Because of the high-bandwidth characteristic of piezoelectric transducers, the piezoelectric impedance can be measured in high frequency range with small wavelengths, which is very promising for detecting and identifying small-sized damage. Modeling piezoelectric impedance in high frequency range, meanwhile, naturally leads to high mesh density as well as large number of unknown parameters to be identified as damage may occur in any elements/segments in the structure. As such, the inverse problem may be under-determined since the number of high-quality measurements is generally limited. One possible strategy is to incorporate additional constraints/criteria in problem formulation. That is, we can generally assume that damage occurs within a limited number of element/segments, so the damage index vector, the dimension of which is the number of segments to be identified, is sparse. In general, damage occurrence in engineering structures is a small probability event. The occurrence of damages at multiple locations simultaneously has even smaller probability. This will lead to a multi-objective optimization problem where one objective

is the minimization of the difference between piezoelectric impedance measurements and the model prediction in the parametric space, and another objective is the sparsity of the damage index vector. Solving this multi-objective optimization problem can lead to a set of solutions which can help pinpointing actual damage using engineering judgment or additional sensing devices. Obviously, the diversity and completeness of the solution set become critically important so the true damage scenario can be included. Here, in this research, we examine systematically how the proposed reinforcement learning hyper-heuristic in multi-objective simulated annealing can effectively tackle the challenges.

The rest of the paper is organized as follows. Section 2 outlines the algorithmic foundation, including the multi-objective simulated annealing algorithm (MOSA) and the reinforcement hyper-heuristic strategy. Section 3 proposes four low-level heuristics embedded in the hyper-heuristic MOSA that combines reinforcement hyper-heuristics with the MOSA algorithm. In Sect. 4, benchmark case studies involving 14 test functions are conducted and analyzed with performance metrics, the inverted generational distance (IGD) and hypervolume (HV), which showcases the performance improvement. Section 5 presents the application of the proposed algorithm on structural damage identification where solution diversity and completeness are essential. Finally, concluding remarks are given in Sect. 6.

2 Algorithm foundation

2.1 Multi-objective optimization and simulated annealing

A multi-objective minimization problem can be expressed as

$$\min \mathbf{y} = f(\mathbf{x}) = \left(f_1(\mathbf{x}), \ldots, f_n(\mathbf{x})\right), \tag{1}$$

where $\mathbf{x} = \left(x_1, \ldots, x_m\right) \in \Omega_x$ is the m-dimensional design variable vector and $\mathbf{y} = \left(y_1, \ldots, y_n\right) \in \Omega_y$ is the n-dimensional objective vector. Ω_x is the feasible domain which is defined by a set of equalities and inequalities of $\boldsymbol{x}$, and Ω_y is the corresponding objective space. Since the objectives of such a problem may conflict with each other, there may not exist a single solution simultaneously optimizing all objectives. Instead, a number of solutions can be obtained with trade-offs between different objectives, known as the Pareto optimal solutions. To evaluate the solutions, the concept of Pareto dominance can be applied. Mathematically, $\mathbf{x}_1$ is said to dominate another solution $\mathbf{x}_2$ (defined as $\mathbf{x}_1 \prec \mathbf{x}_2$) if: $f_i\left(\mathbf{x}_1\right) \le f_i\left(\mathbf{x}_2\right), \forall i \in \{1, 2, \ldots, n\}$ and $f_j\left(\mathbf{x}_1\right) < f_j\left(\mathbf{x}_2\right), \exists i \in \{1, 2, \ldots, n\}$. When there does not exist another solution that dominates $\mathbf{x}^* \in \Omega_x$, then it becomes a non-dominated solution, i.e., Pareto optimal and is included into Pareto optimal set.

Several metaheuristics have been developed to solve the multi-objective optimization problem, such as evolutionary algorithm (Zhou et al. 2011), genetic algorithm (Deb et al. 2000]), particle swarm algorithm (Mohd et al. 2018), and simulated annealing, etc. While these approaches have been widely applied, simulated annealing has shown interesting versatility and adaptivity. Simulated annealing mimics the metallurgical process of annealing during which a heated metal is cooled to the ground state. Multi-objective Simulated Annealing (MOSA) is a class of simulated annealing extensions to multi-objective optimization, exploiting the idea of constructing an estimated Pareto front by gathering non-dominated solutions found while exploring the feasible domain. In MOSA, the acceptance criteria are traditionally derived by adopting the differential between new and current solutions. However, the comparison between the new solution to the current solution remains to be an issue. Therefore, several new techniques have been proposed by using Pareto domination-based acceptance criterion (Smith 2006; Bandyopadhyay et al. 2008; Cao et al. 2019). The domination status of the point is considered with respect to the current solution together with the archive of non-dominated solutions. MOSA can find multiple Pareto-optimal solutions in a single run.

2.2 Reinforcement learning hyper-heuristics

The reinforcement learning hyper-heuristic strategy proposed in this research consists of two parts, heuristic selection and credit assignment. Essentially, we want to design online strategies that are capable of autonomously selecting between different heuristics based on their credits (Burke et al. 2013). The credit assignment firstly rewards the heuristics online based on the specific criterion, and then the credits are fed to the heuristic selection strategy. Fundamentally, this is analogous to the reward assignment in reinforcement learning, where the agent receives a numerical reward based on a successful action. Here, in this research, a new credit assignment strategy is developed based on hypervolume (Zitzler and Thiele 1999) increments as well as the number of solutions newly generated to calculate the credit $c_{i,t}$

$$c_{i,t} = e^{\frac{i(t)}{iter}} \cdot \left(\frac{\frac{(HV(PF_t) - HV(PF_{t-1}))}{HV(PF_{true})} + \frac{|PF_t| - |\bigcap(PF_t, PF_{t-1})|}{|PF_t|}}{i(t) - i(t-1)} \right) \tag{2}$$

In the above Equation, *iter* is the total number of iterations, $i(t)$ is the number of iterations that has been performed at epoch t (i.e., the t-th time heuristic selection has been conducted), PF_t represents the Pareto front at t, and $HV(*)$ approximates the hypervolume of the Pareto front in percentage using Monte Carlo approach through N uniformly distributed samples

within the bounded hyper-cuboid to alleviate the computational burden. Specifically,

$$HV(PF, r*) = volume(\bigcup_{x \in PF} v(x, r*)), \tag{3}$$

where r^* is the reference point, which is set to be 1.1 times the upper bound of the Pareto front in the HV calculation (Ishibuchi et al. 2010; Li et al. 2016). Therefore, in Eq. (2), $HV(PF_t) \in [0, 1]$ is the hypervolume of the Pareto front at t, $(HV(PF_t) - HV(PF_{t-1}))$ is the hypervolume increment since the last time the heuristics are selected, and $HV(PF_{true})$ is the normalization term. The term $\left(|PF_t| - |\bigcap (PF_t, PF_{t-1})|\right)/|PF_t| \in [0, 1]$ computes the percentage of the newly generated solution in the current Pareto front. Both terms are dimensionless, and they are summed together first then divided by $(i(t) - i(t-1))$ to evaluate the performance of a heuristic as reflected by the evolution of the Pareto front per iteration. Because it is easier for the optimizer to achieve improvements at early stage of optimization, we introduce the compensatory factor $e^{i(t)/iter} \in [1, e]$ to emphasize the credits earned as the optimization progresses progressively.

Heuristic selection starts from the low-level heuristics at each time epoch. The concept is similar to agent in reinforcement learning. There is, however, the exploration versus exploitation dilemma (EvE). That is, while the heuristic with the highest credits should be favored, those with low credits need to be selected because they may lead to high-quality results. Previous strategies include probability matching (PM), adaptive pursuit (Thierens 2007), choice function (Cowling et al. 2000; Maashi et al. 2015), Markov chain models (McClymont and Keedwell 2011), and multi-armed bandit algorithms (Krempser et al. 2012). Here, we formulate a heuristic selection strategy with a minimal number of parameters inspired by the idea of probability matching to specifically fit the online learning scheme. Given a finite set of heuristic $\mathbf{O}$, an heuristic $o_i \in \mathbf{O}$ is selected at time t with probability $p_{i,t}$ proportional to the quality of heuristic $q_{i,t}$, which is mainly determined by the credit $c_{i,t}$. The parameter t is independent of the algorithm, indicating how many times the heuristic selection has been conducted. The update rule is given as follows:

$$q_{i,t} = \alpha \cdot q_{i,t-1} + (1 - \alpha) \cdot c_{i,t} \tag{4}$$

$$p_{i,t} = p_{\min} + (1 - |\mathbf{O}| \cdot p_{\min}) \frac{q_{i,t}}{\sum_{j=1}^{|\mathbf{O}|} q_{j,t}}, \tag{5}$$

where $p_{\min} \in (0, \frac{1}{|\mathbf{O}|}]$ is the minimum selection probability to facilitate exploration and guarantee $p_{i,t} \in [0, 1]$. It is greater than 0 so that the heuristics with low credits are also considered. Here, in our research, the value of $p_{\min}$ is tuned to a relatively small value of 0.1 for the following considerations: (1) larger value of $p_{\min}$ will negatively affect the selection of heuristics with high credits (i.e., heuristics with good performance) to which more attention should be still paid; (2) when larger value is given to select heuristics with low credits, the exploration will take long time, thus resulting in longer computing time for convergence. Our subsequent case studies demonstrate that this selection leads to good performance in general. Meanwhile, the forgetting factor $\alpha \in [0, 1]$ determines the significance of the credits received previously because the current solution may be the result of a decision taken in the past. If $\alpha > 0.5$, the algorithm will focus more on previous credits obtained; and if $\alpha < 0.5$, it will focus more on current credits, as indicated in Eq. (4). Here, we take the previous and current credits with equal importance, so the value of α is set as 0.5. Note that the credit means the algorithm will reward the heuristic due to its generation of solutions with high quality. It is worth noting here again that $t - 1$ in Eq. (4) does not imply the iteration before t in optimization; it means the last time the hyper-heuristic is updated. And we only update the values that correspond to the chosen heuristic at $t - 1$. For unselected heuristics, we have $q_{i,t} = q_{i,t-1}$. In order to facilitate the algorithm, the value of $q_{i,0}$ is set as 0.1 at the beginning of the computation and will be updated after iterations. After $p_{i,t}$ is determined using Eqs. (4) and (5), roulette wheel selection method (Lipowski and Lipowska 2012) is used to choose the lower-level heuristic per its probability.

3 Hyper-heuristic MOSA

Based on the hyper-heuristic rules defined, the MOSA algorithm and the joint hyper-heuristic scheme are presented in this section.

3.1 MOSA/R algorithm

Hereafter, the algorithm used in this study is referred to as Multi-Objective Simulated Annealing based on Re-seed (MOSA/R), which was originally explored for configuration optimization (Cao et al. 2019). MOSA/R computes the acceptance probability of a new solution using the concept of the amount of domination. The algorithm was designed, aiming at solving multimodal optimization problems with strong constraints. It takes care of feasible solutions more efficiently due to the re-seed technique developed compared to traditional MOSAs. As will be demonstrated in this research, the advancement of MOSA/R can be generalized with hyper-heuristics by making the re-seed step autonomously to cater to various design preferences. The pseudocode of MOSA/R is provided as shown in Algorithms 1–5.

Algorithm 1 MOSA/R

Set $Tmax$, $Tmin$, # of iterations per temperature $iter$, cooling rate α, $k = 0$
Initialize the *Archive* (Pareto front)
current solution = randomly chosen from *Archive*
while $T > Tmin$ **do**
    for 1:*iter* **do**
        Generate a *new solution* in the neighborhood of *current solution*
        if *new solution* dominates $k(k >= 1)$ solutions in the *Archive* **then**
            Update
        else if *new solution* dominated by k solutions in the *Archive* **then**
            Action
        else if *new solution* non-dominant to *Archive* **then**
            Action
        end if
    end for
end while

Algorithm 2 Update

Remove all k dominated solutions from the *Archive*
Add *new solution* to the *Archive*
Set *new solution* as *current solution*

Algorithm 3 Action

if *new solution* and *Archive* are non-dominant to each other **then**
    Set *new solution* as *current solution*
else
    if *new solution* dominated by *current solution* **then**
        Re-seed
    else
        Simulated Annealing
    end if
end if

Algorithm 4 Re-seed

new solution dominated by $k(k >= 0)$ solutions in the *Archive*
Select a heuristic from **low-level heuristics** based on hyper-heuristic strategy
Set *selected solution* following the selected **heuristic**
if $1/\left(1 + e^{-\frac{\Delta dom_{selected,new}}{\max(T,1)}}\right) > rand\,(0,1)$ **then**
    Set *selected solution* as *current solution*
else
    Simulated Annealing
end if

Algorithm 5 Simulated Annealing

1: $\Delta dom_{avg} = \frac{\sum_{i=1}^{k} \Delta dom_{i,new}}{k}$
2: **if** $\frac{1}{\left(1+e^{\frac{\Delta dom_{avg}}{T}}\right)} > rand\,(0,1)$ **then**
3: Set *new solution* as *current solution*
4: **end if**

Given two solutions **a** and **b**, if $\mathbf{a} \prec \mathbf{b}$ (i.e., **a** dominates **b**) then the amount of domination is defined as

$$\Delta dom_{\mathbf{a},\mathbf{b}} = \prod_{i=1, f_i(\mathbf{a}) \neq f_i(\mathbf{b})}^{M} \left(\left|f_i(\mathbf{a}) - f_i(\mathbf{b})\right| / R_i\right), \tag{6}$$

where M is the number of objectives, and R_i represents the range of the ith objective (Bandyopadhyay et al. 2008). The hyper-heuristic scheme comes into effect in Algorithm Re-seed, as indicated in the pseudo-code Algorithm 4. Whenever re-seed is triggered, a low-level heuristic is firstly selected from the repository based on the proposed reinforcement learning hyper-heuristic (Sect. 2.3), and then the current solution is altered using the selected low-level heuristic. Simulated annealing in most related hyper-heuristic studies (Antunes et al. 2011; Bai et al. 2012; Burke et al. 2013;) is used as the high-level heuristic to select lower-level heuristic from the repository to exploit multiple neighborhoods, which can be regarded as variable neighborhood search mechanism. However, the proposed approach in this research uses probability matching (PM) as the high-level heuristic and part of the MOSA/R as lower-level heuristics, which can be regarded as an adaptive operator selection (Maturana et al. 2009). In the next subsection, we propose four low-level heuristics for the hyper-heuristic MOSA/R.

3.2 Low-level heuristics

Hereafter, the MOSA/R with the hyper-heuristic scheme is referred to as MOSA/R-HH. The hyper-heuristic scheme intervenes in the re-seed scheme (Algorithm Re-seed), which makes itself different from other MOSA algorithms. In this paper, we propose four re-seed strategies as low-level heuristics.

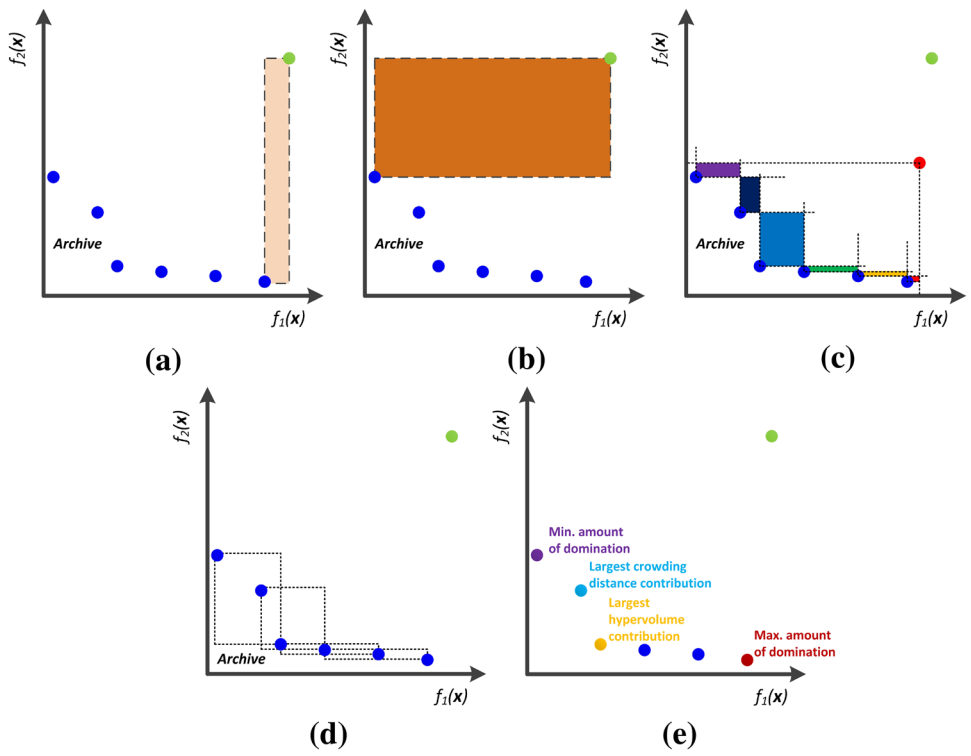

Fig. 1 Examples of solutions selected by the four low-level heuristics

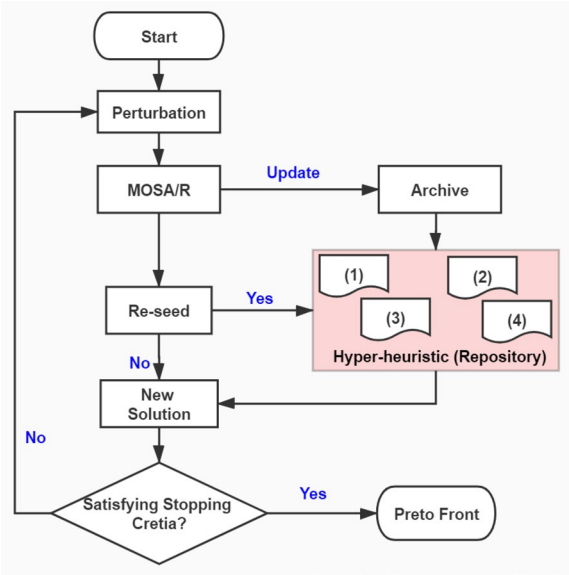

Fig. 2 Flowchart of MOSA/R and the embedded hyper-heuristic

(1) Minimum amount of domination of solution in the *Archive*. The first strategy selecting the solution from *Archive* calculates the minimum difference of domination amount with respect to the new solution. For $\forall \mathbf{x} \in Archive$ that dominates the *new solution*,

$$\begin{aligned}\mathbf{x}_{select} &= \arg\min_{\mathbf{x}}(\Delta dom_{\mathbf{x},\mathbf{x}_{new}}) \\ &= \arg\min_{\mathbf{x}}\left(\prod_{i=1,f_i(\mathbf{x})\neq f_i(\mathbf{x}_{new})}^{M}(|f_i(\mathbf{x})-f_i(\mathbf{x}_{new})|/R_i)\right).\end{aligned} \tag{7}$$

Then the selected solution is set as current solution with probability $\frac{1}{1+\exp(-\Delta dom_{selected,\,new}/\max(T,1))}$. To avoid premature convergence, the solution is chosen with the minimum difference of domination amount. As shown in Fig. 1(a), the selected solution using this strategy corresponds to the one in the *Archive* that dominates the current solution the least.

(2) Maximum amount of domination of solution in the *Archive*. The second strategy is defined similarly to low-level heuristic (1). For $\forall \mathbf{x} \in Archive$ that dominates the new solution,

$$\begin{aligned}\mathbf{x}_{select} &= \arg\max_{\mathbf{x}}(\Delta dom_{\mathbf{x},\mathbf{x}_{new}}) \\ &= \arg\max_{\mathbf{x}}\left(\prod_{i=1,f_i(\mathbf{x})\neq f_i(\mathbf{x}_{new})}^{M}(|f_i(\mathbf{x})-f_i(\mathbf{x}_{new})|/R_i)\right).\end{aligned} \tag{8}$$

The only difference is that this time the solution will be chosen with the maximum domination amount compared to the new solution. The strategy emphasizes the exploitation of better neighboring solutions than strategy (1) that aims to maintain a balance between exploration and exploitation. As shown in Fig. 1(b), the selected solution by the second strategy dominates the current solution the most. The first two strategies are new solution dependent. Next, we will introduce two new solution-independent strategies.

(3) Solution with the largest hypervolume (HV) contribution in the *Archive*. In this heuristic, the hypervolume contribution of each point in *Archive* is computed using the method proposed by Emmerich et al (2005). Hypervolume contribution quantifies how much each point in the Pareto front contributes to the HV. As explained in Fig. 1(c), the areas of the colored rectangles indicate the hypervolume contribution for each solution in the Archive. A large value of HV contribution indicates that the point stays in a less explored portion of the Pareto front but with good convergent performance.

Table 1 Main properties of the 14 test functions

Problem	No. of Obj	No. of Var	Properties
DTLZ1	3	6	Linear Pareto, multimodal
DTLZ2	3	7	Concave Pareto
DTLZ3	3	10	Concave Pareto, multimodal
DTLZ4	3	10	Concave Pareto, biased solutions distribution
DTLZ5	3	10	Concave degenerated Pareto
DTLZ6	3	10	Concave Pareto, biased solutions distribution
DTLZ7	3	10	Discontinuous Pareto
UF1	2	10	Convex Pareto
UF2	2	10	Convex Pareto
UF3	2	10	Convex Pareto
UF4	2	10	Concave Pareto
UF5	2	10	Discrete Pareto
UF6	2	10	Discontinuous Pareto,
UF7	2	10	Linear Pareto

(4) Solution with the largest crowding distance in the *Archive*. This strategy utilizes the technique called crowding distance (Deb et al. 2002a b), and the point will be selected with the largest crowding distance. The strategy is inclined to exploration (diversity) in the EvE dilemma. As presented in Fig. 1(d), in the minimization case, the crowding distance for each solution in the *Archive* is determined by the area of the bounding box formed by its adjacent solutions. It is worth noting that, in computing crowding distance, the edge points (min/max points) are set as infinity after sorting operation based on objective values. Figure 1(d) is employed for illustration only, and the infinite edge points are not included.

Figure 1(e) compares the solutions selected by the proposed four low-level heuristics, each low-level heuristic design has its own emphasis and intention. The hyper-heuristic scheme is designed to adaptively switch between different priorities that suit the current search endeavor the best, and therefore could be applied to tackle different instances without further modification. Figure 2 depicts the overall mechanism of MOSA/R and the co-acting hyper-heuristic in a flowchart.

4 Benchmark case studies

4.1 Test cases

The proposed algorithm MOSA/R-HH, AMOSA (Bandyopadhyay et al. 2008), NSGA-II (Deb et al. 2002a b), and MOEA/D (Zhang and Li 2007) algorithms are applied here to evaluate the benchmark test problems including DTLZ (Deb et al. 2002a b) and UF (Zhang et al. 2008) test suites. These three algorithms are selected here for comparison because they have been applied to a number of multi-objective optimization problems. As listed in Table 1, the test functions are representative due to their diverse properties. All algorithms will be executed 5 times independently for each test problem.

4.2 Parametric setting

The initial temperature and final temperature (stopping criterion) control the acceptance of all solutions at the beginning of the algorithm (Suman and Kumar 2006) and error, respectively. The starting temperature T_{max} and final temperature T_{min} values for AMOSA and MOSA/R-HH are here set to be 100 and 10^{-5}, respectively. The total number of iterations, denoted as *iter*, is chosen to be 20,000 for DTLZ1 and DTLZ2, 30,000 for DTLZ3-7, and 100,000 for UF test problems. For the cooling process in simulated annealing, the exponential approach is adopted as $T_{i+1} = \alpha^i T_i$ with cooling coefficient of 0.8. Note that all parameters in AMOSA are set to be the same as that of MOSA/R-HH. For NSGA-II and MOEA/D, the total number of function evaluations is set in accordance with AMOSA and MOSA/R-HH. Other parameters are used following those in literature (Deb et al. 2002a,b; Zhang and Li 2007). The population size is set to be 150 and 300 for 2-objective and 3-objective test problems, respectively. The distribution indices of Simulated Crossover (SBX) and polynomial mutation are set to be 20. The crossover rate is 1.0, and the mutation ration is $1/n$, where n is the length of the decision vector. In MOEA/D, Tchebycheff approach is used, and the size of neighbor population is set to be 20. All initial solutions are generated randomly from the decision space of the problems.

4.3 Performance metrics

In this study, two popular metrics, inverted generational distance (IGD) (Ishibuchi et al. 2015) and hypervolume (HV) (Zitzler et al. 2007), are used to quantify the performance of the algorithms. The performance comparison is based on the Pareto set that it is a set of solutions realizing the optimal trade-offs between the optimization objectives in multi-objective optimization problems.

Inverted Generational Distance (IGD) The IGD indicator measures the degree of convergence by computing the average of the minimum distance of points in the true Pareto front ($PF*$) to points in Pareto front obtained (PF), as described below:

$$IGD(PF, PF*) = \frac{\sum_{\mathbf{f}*\in PF*,\, i=1}^{|PF*|} \sqrt{\min_{\mathbf{f}\in PF} \left(\sum_{m=1}^{M} (f_m^i * - f_m)^2 \right)}}{|PF*|} \tag{9}$$

where M is the number of objectives, f_m is the mth objective value of $\mathbf{f} \in PF$. In Eq. (9), $\min_{\mathbf{f}\in PF} \left(\sum_{m=1}^{M} (f_m^i * - f_m)^2 \right)$ calculates the minimum Euclidean distance between the ith point in $PF*$ and points in PF. A lower value of IGD indicates better convergence and completeness of the PF obtained.

Hypervolume (HV) The HV indicator measures convergence as well as diversity as shown in Eq. (3). The calculation of HV requires normalized objective function values and here HV stands for the percentage covered by the Pareto front of the cuboid defined by the reference point and the original point (0, 0, 0). As mentioned before, the reference point is set to be 1.1 times the upper bound of the $PF*$.

4.4 Test case results and discussions

The four algorithms are applied to the test functions listed in Table 1. The analysis results are based on 5 independent test runs and meanwhile the mean and standard deviation of IGD and HV are recorded. All computations are conducted within

Table 2 Numerical test results: IGD mean and standard deviation

Problems	MOSA/R-HH	AMOSA	NSGA-II	MOEA/D
DTLZ1	0.007191 ± 0.000369	0.02134 ± 0.00506	1.656 ± 0.538	0.01315 ± 0.00195
DTLZ2	0.01403 ± 0.00127	0.01992 ± 0.00107	0.03093 ± 0.00147	0.02434 ± 0.00173
DTLZ3	0.06330 ± 0.00380	0.7198 ± 0.131	7.419 ± 1.87	0.0342 ± 0.0125
DTLZ4	0.02263 ± 0.00222	0.07643 ± 0.00456	0.02176 ± 0.000668	0.02334 ± 0.00176
DTLZ5	6.356E-4 ± 4.34E-5	0.001956 ± 1.49E-4	0.001390 ± 2.74E-4	0.002541 ± 0.0966
DTLZ6	3.231 E-4 ± 5.42E-6	4.404E-4 ± 1.85E-4	0.8738 ± 0.0762	0.001792 ± 2.20E-4
DTLZ7	0.01657 ± 9.49E-4	0.01928 ± 5.45E-4	0.8235 ± 0.0211	0.06502 ± 0.00152
UF1	0.01252 ± 0.00189	0.03509 ± 0.00250	0.01972 ± 0.00967	0.01938 ± 0.00567
UF2	0.002974 ± 6.25E-4	0.005458 ± 8.87E-05	0.006871 ± 0.00365	0.01876 ± 0.00563
UF3	0.2477± 0.104	0.3797 ± 0.368	0.1559 ± 0.0131	0.2553 ± 0.0323
UF4	0.01905 ± 8.76E-4	0.03124 ± 1.99E-4	0.03792 ± 0.00397	0.04796 ± 0.00513
UF5	0.1636 ± 0.00666	0.1523 ± 0.0242	0.6759 ± 0.279	0.6501 ± 0.292
UF6	0.1412 ± 0.0816	0.09371 ± 4.34E-06	0.4929 ± 0.0963	0.5606 ± 0.151
UF7	0.01713 ± 1.33 E-4	0.03393 ± 0.00514	0.008407 ± 0.00309	0.005269 ± 5.043E-4

MATLAB on a desktop computer with Intel(R) Core(TM) i7-10700F CPU @ 2.90 GHz, 16 G RAM.

Tables 2 and 3 show the relative performance of all four algorithms in terms of the two metrics IGD and HV, where we keep 4 significant digits for mean and standard deviation. The shaded grids indicate the best result in each test in terms of the mean value. As can be observed from the table, MOSA/R-HH prevails in DTLZ1, DTLZ2, DTLZ5, and DTLZ7 in both metrics. MOEA/D has an edge over MOSA/R-HH in DTLZ3, while MOSA/R-HH performs significantly better than NSGA-II and AMOSA. DTLZ4 is a close race for MOSA/R-HH, NSGA-II, and MOEA/D. And for DTLZ6, MOSA/R-HH, AMOSA, and MOEA/D all demonstrate similar performance. Figure 3 depicts the Pareto front obtained by each algorithm when applied to DTLZ1 test case. It is worth noting that different algorithms may exhibit different strengths in specific cases. Consider DTLZ3 as an example. DTLZ3 involves the Rastrigin function, a non-convex, non-linear multimodal function, on top of DTLZ2, which is employed to test the convergence to the true Pareto front. MOEA/D essentially decomposes multiple objectives into multiple single objectives. As such, it is possible to avoid certain limitations of the evolutionary algorithms based on the Pareto dominant relationship, which is similar to the MOSA/R-HH algorithm. Therefore, in certain cases the convergence of MOEA/D algorithm to the true Pareto front may indeed be on par or even better. This, however, does not change the main observation here that MOSA/R-HH mostly outperforms other algorithms.

For UF test cases, MOSA/R-HH takes the lead in three of them in both IGD and HV, which is the best among the four algorithms. Figure 4 shows an example of the Pareto front obtained by each algorithm for UF4 in comparison with the true Pareto front. It can be noticed that the Pareto

Table 3 Numerical test results: HV mean and standard deviation

Instance	MOSA/R-HH	AMOSA	NSGA-II	MOEA/D
DTLZ1	0.8593 ± 0.0204	0.8312 ± 0.0184	0.04210 ± 0.0941	0.8353 ± 0.0282
DTLZ2	0.5945 ± 0.00586	0.5850 ± 0.00130	0.5663 ± 0.00832	0.5789 ± 0.00420
DTLZ3	0.5280 ± 0.0380	0.004466 ± 0.00470	0.001404 ± 0.00236	0.5376 ± 0.0248
DTLZ4	0.5739 ± 0.00869	0.5535 ± 0.00738	0.5686 ± 0.00765	0.5763 ± 0.00877
DTLZ5	0.2139 ± 0.00157	0.2096 ± 0.00125	0.2097 ± 0.00100	0.2038 ± 0.00356
DTLZ6	0.2059 ± 0.00568	0.2029 ± 0.00166	0.001440 ± 0.00211	0.2012 ± 0.00119
DTLZ7	0.2635 ± 0.00549	0.2580 ± 0.0122	0.1683 ± 0.00304	0.2498 ± 0.00557
UF1	0.7114 ± 0.00231	0.683 ± 0.00198	0.6958 ± 0.0126	0.6962 ± 6.37E-4
UF2	0.7207 ± 5.52 E-4	0.71843 ± 4.03E-4	0.7165 ± 0.00351	0.7036 ± 0.00355
UF3	0.4724 ± 0.0993	0.4098 ± 0.227	0.5196 ± 0.0204	0.3787 ± 0.0454
UF4	0.4224 ± 0.00295	0.4044 ± 0.00659	0.3919 ± 0.00760	0.3885 ± 0.0131
UF5	0.3613 ± 0.0346	0.3651 ± 0.0405	0.05647 ± 0.0524	0.1128 ± 0.158
UF6	0.3287 ± 0.0428	0.3487 ± 0.00766	0.1104 ± 0.0413	0.2214 ± 0.0643
UF7	0.5677 ± 0.00127	0.5454 ± 0.00541	0.5734 ± 0.00451	0.5773 ± 0.00169

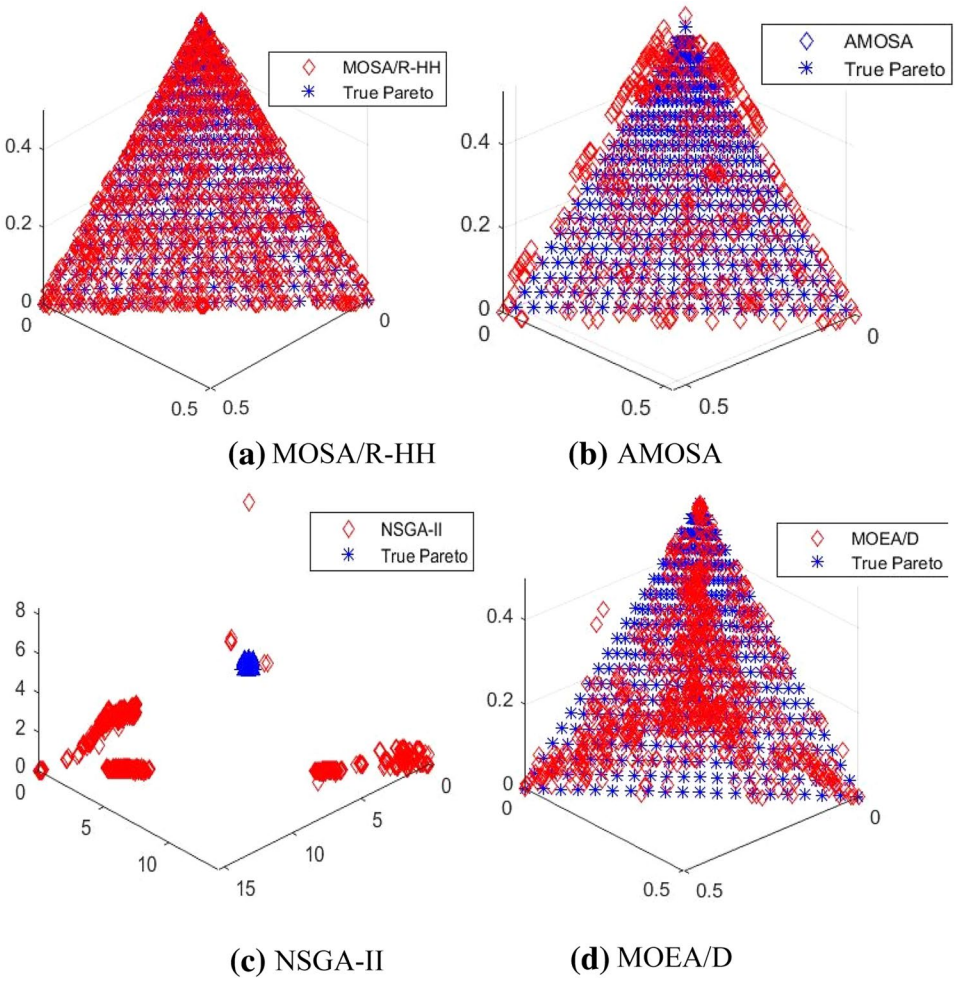

Fig. 3 Pareto front obtained by each algorithm for test instance DTLZ1

front obtained by MOSA/R-HH stays close to the true Pareto front and maintains good diversity. The performance of AMOSA, NAGA-II, and MOEA/D fluctuate as test function changes due to different problem properties. On the other hand, MOSA/R-HH is more robust and outperforms other algorithms when tackling most test instances because of the adaptive hyper-heuristic scheme.

5 Application to structural damage identification

In this section, we apply the proposed approach (MOSA/R-HH) to the identification of damage parameters in a structure based on piezoelectric impedance/admittance active interrogation, to showcase the advantage of incorporating the hyper-heuristic technique in engineering implementation.

5.1 Piezoelectric impedance/admittance for structural damage identification

Structural damage identification, i.e., the process of identifying the location and severity of damage, is typically realized by inverse analysis through comparison between sensor measurements and model prediction in the parametric space. Active interrogation through actuation and sensing is widely adopted. Piezoelectric transducers are compact and can be easily integrated with the host structure. Owing to the two-way electromechanical coupling, they can be used as actuators and/or sensors. They possess high bandwidth, and thus can be used for high-frequency active interrogation which is promising for detecting small-sized damage. The finite element-based equations of motion of a structure integrated with a piezoelectric transducer can be derived as (Wang and Tang 2008)

$$\mathbf{M}\ddot{\mathbf{x}}+\mathbf{C}\dot{\mathbf{x}}+\mathbf{K}\mathbf{x}+\mathbf{K}_{12}Q=\mathbf{0} \tag{10}$$

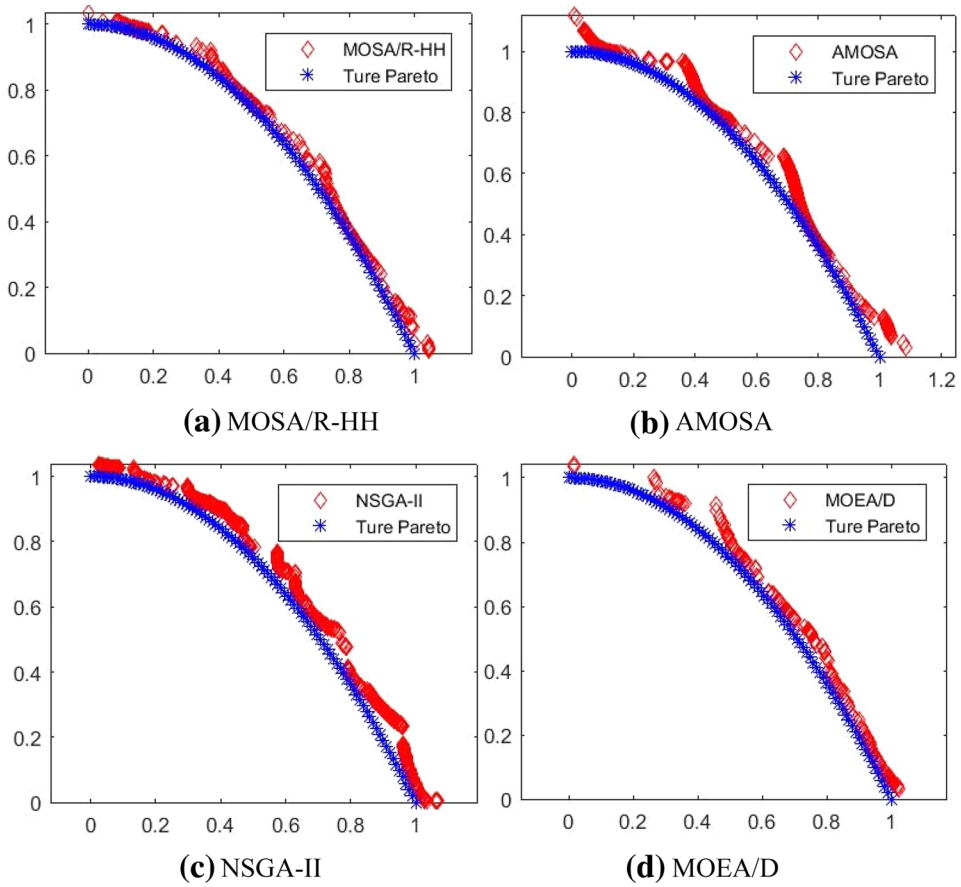

Fig. 4 Pareto front obtained by each algorithm for test instance UF4

$$K_c Q + \mathbf{K}_{\mathbf{12}}^{\mathbf{T}}\mathbf{x} + R\dot{Q} = V_{in}, \tag{11}$$

where $\mathbf{x}$ is the structural displacement vector, $\mathbf{M}$, $\mathbf{K}$, and $\mathbf{C}$ are mass, stiffness and damping matrices, respectively,$\mathbf{K}_{12}$ is the electro-mechanical coupling vector, K_c is the reciprocal of capacitance of the piezoelectric transducer, R is the resistor employed in the measurement circuit, Q is the electrical charge on the surface of piezoelectric transducer, and V_{in} is the input/excitation voltage. In the context of structural damage identification, the host structure is divided into n segments. We assume damage occurs in one or some of the segments as local stiffness reduction. Here, without loss of generality, we assume damage in structure causes stiffness reduction while the mass remains unchanged. The stiffness matrix of the damaged structure can be written as $\mathbf{K}_d = \sum_{j=1}^{n} \mathbf{K}_{hj}\left(1 - \alpha_j\right)$, where $\mathbf{K}_{hj}$ is the stiffness matrix of the jth segment of the healthy structure, α_j is the damage index indicating damage severity $\left|\alpha_j\right|$ and location j. In structural damage identification, we aim at identifying $\boldsymbol{\alpha} = [\alpha_1, \cdots, \alpha_n]$ which is referred to as the damage index vector.

While a variety of active interrogation approaches have been proposed, in this research, we apply the piezoelectric impedance/admittance approach. In actual practice, we supply frequency-sweeping excitation voltage to the piezoelectric transducer integrated with the host structure and measure the resulting current in the circuit. After derivations, we can obtain, for example, the admittance of the integrated system (Shuai et al. 2017; Cao et al. 2018b):

$$A(\omega) = \frac{\bar{I}}{\bar{V}_{in}} = \frac{i\omega}{i\omega R + K_c - \mathbf{K}_{\mathbf{12}}^{\mathbf{T}}\left(\mathbf{K}_d - \omega^2\mathbf{M} + i\omega\mathbf{C}\right)^{-1}\mathbf{K}_{12}}, \tag{12}$$

where ω is the excitation frequency, i is the imaginary unit, and $\bar{I}$ and $\bar{V}_{in}$ are, respectively, the magnitude of the current and that of the voltage input. Although both impedance and admittance which is the reciprocal of the impedance have been used in previous investigations, here in this research, we focus on the admittance. In piezoelectric impedance or admittance based active interrogation, the same piezoelectric transducer is used as actuator and sensor concurrently, which leads to implementation convenience. Moreover, as impedance and admittance are harmonic responses, the inverse analysis is more likely to be realized than transient responses. In order to facilitate efficient computational analysis, we conduct linearization of Eq. (12) to develop

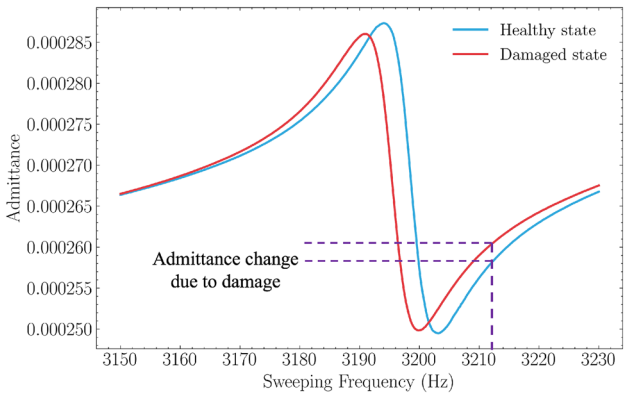

Fig. 5 Illustration of admittance responses and admittance change due to damage

The admittance changes then can be written as a linear function of the damage index α_j.

$$\Delta A(\omega) = A_d - A(=\mathbf{0}) = \sum_{j=1}^{n} [\omega i (K_c - \mathbf{K}_{12}^T \mathbf{Z}^{-1} \mathbf{K}_{12})^{-2} \mathbf{K}_{12}^T \mathbf{Z}^{-1} (\mathbf{L}_j^T \mathbf{K}_{hj} \mathbf{L}_j) \mathbf{Z}^{-1} \mathbf{K}_{12}] \alpha_j, \tag{15}$$

where $\mathbf{Z} = \mathbf{K} - \mathbf{M}\omega^2 + i\omega\mathbf{C}$ denotes the dynamic stiffness of the structure and $\mathbf{L}$ indicates how the elemental matrices are assembled into the global stiffness matrix. Equation (15) exhibits the relationship between the admittance changes and damage index at single excitation frequency point ω. Such relationship holds at every frequency point of voltage excitation. When admittances are measured at m frequency points, m equations can be formulated to establish the relation as a matrix form

$$\Delta \mathbf{A} = \begin{bmatrix} \Delta A(\omega_1) \\ \vdots \\ \Delta A(\omega_m) \end{bmatrix} = \frac{i\omega \left(\left(\mathbf{K} - \omega^2 \mathbf{M} + i\omega \mathbf{C} \right)^{-1} \mathbf{K}_{12} \right)^T \mathbf{L}^T \mathbf{K}_h \mathbf{L} \left(\left(\mathbf{K} - \omega^2 \mathbf{M} + i\omega \mathbf{C} \right)^{-1} \mathbf{K}_{12} \right)}{\left(K_c + i\omega R - \mathbf{K}_{12}^T \left(\mathbf{K} - \omega^2 \mathbf{M} + i\omega \mathbf{C} \right)^{-1} \mathbf{K}_{12} \right)^2} = \mathbf{S}_{m \times n} \boldsymbol{\alpha}. \tag{16}$$

a sensitivity-based relation between the admittance change and the damage index vector (Shuai et al. 2017),

$$A_d(\boldsymbol{\alpha}) \approx A(\boldsymbol{\alpha} = \mathbf{0}) + \sum_{j=1}^{n} \frac{\partial A}{\partial \alpha_j}|_{\alpha_j = 0} \alpha_j, \tag{13}$$

where

$$\frac{\partial A}{\partial \alpha_j}|_{\alpha_j = 0} = \omega i [i\omega R + K_c - \mathbf{K}_{12}^T (\mathbf{K} - \mathbf{M}\omega^2 + \mathbf{C}\omega i)^{-1} \mathbf{K}_{12}] - {}^{-2}\mathbf{K}_{12}^T [\frac{\partial (\mathbf{K}_d - \mathbf{M}\omega^2 + \mathbf{C}\omega i)^{-1}}{\partial \alpha_j}|_{\alpha_j = 0}] \mathbf{K}_{12}. \tag{14}$$

In the above equation, $\Delta \mathbf{A}(\boldsymbol{\omega}) = \mathbf{A}_d(\alpha \neq 0) - \mathbf{A}(\alpha = 0)$ represents the vector of the changes of admittance at a series of excitation frequency points where admittance is measured. For example, we can measure admittance at m frequency points $\omega_1, \ldots, \omega_m$ and then obtain the admittance change vector before and after damage occurrence. $\mathbf{S}_{m \times n}$ is the sensitivity matrix in terms of the coefficient matrices shown in Eq. (16). An example of admittance response and the change are illustrated in Fig. 5. Our mission is to solve for $\boldsymbol{\alpha}$ based on the admittance change vector and the sensitivity matrix $\mathbf{S}_{m \times n}$.

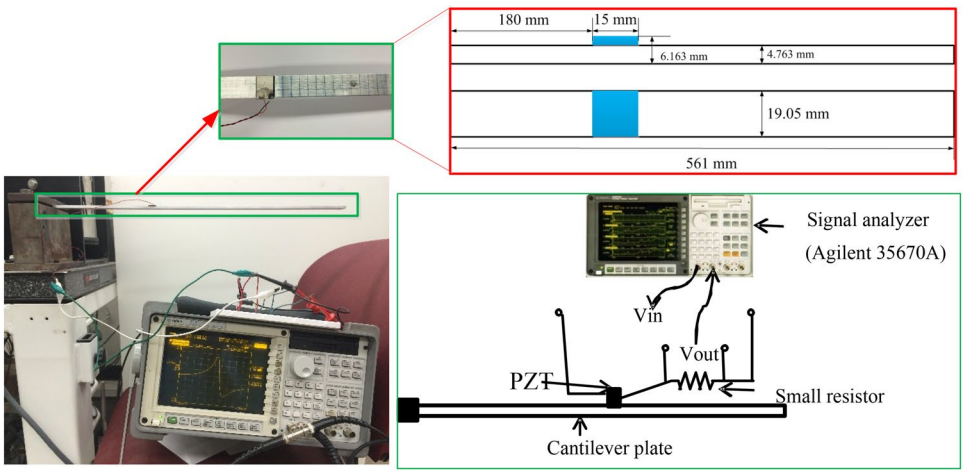

Fig. 6 Experimental setup and geometry of cantilever plate

5.2 Inverse optimization formulation

As can be seen in Fig. 5, admittance changes are more significant around the peaks which correspond to the structural resonances. The changes are much less significant elsewhere and can be easily contaminated by measurement noise. One can envision that the effective measurements with noticeable changes are generally limited. That is, m is small. Meanwhile, to inversely identify small-sized damage, the number of finite elements and the number of segments will need to be large such that the analysis can have high fidelity in high frequency range and the damage can be pinpointed. As such, the number of segments or the dimension of the damage index vector, n, will need to be large. Moreover, it is important to point out that the rows of the sensitivity matrix are not necessarily linearly independent, as the selection of frequency points for admittance measurement is generally arbitrary, e.g., evenly distributed with the frequency range of interest. Therefore, the inverse problem, Eq. (18), is oftentimes under-determined.

In order to solve the structural damage identification problem, here we cast the inverse analysis into an optimization framework. One objective is obvious, i.e., to minimize the difference between measurements and model prediction in the damage parametric space. In this research, we impose an additional objective that fits the nature of damage identification. In engineering practice, structural damage occurrence is normally a small probability event. The occurrence of damages at multiple locations has very small probability. That is, we can assume the number of segments with damage is small or, equivalently speaking, the damage index vector is sparse. This fits the nature of damage occurrence in practical situations. We then have the following optimization model:

$$\begin{cases} \text{find } \boldsymbol{\alpha} \in \mathbf{E}^n \\ \min \ \|\Delta A - \Delta A_{meas}\|_2 \\ \min \ \|\boldsymbol{\alpha}\|_0 \\ \text{s.t.} \alpha_l \leq \alpha_j \leq \alpha_u \end{cases} \tag{17}$$

Here, α_l is the lower bound of the damage index with value of 0, indicating healthy state, and α_u is upper bound with value of 1, meaning totally damaged state, and $\|\|_p$ denotes the l_p norm. It is worth emphasizing that for the multi-objective optimization formulated in Eq. (17), we may expect multiple solutions of damage index vector $\boldsymbol{\alpha}$, which fits the situation that the inverse problem in structural damage identification is under-determined. If multiple solutions are indeed found, we may use engineering judgment or deploy additional sensors for final decision making. In comparison, a single objective optimization generally yields a single solution, which may not reflect the actual damage scenario.

5.3 Experimental setup

We conduct finite element formulation and experiment to generate necessary data for case demonstration. The setup is shown in Fig. 6. A cantilever plate is used as the host structure with the length 561 mm, width 19.05 mm, and thickness 4.763 mm. It is made of aluminum with mass density 2700 kg/m^3 and Young's modulus 68.9 GPa. A piezoelectric transducer is attached to the top surface at 180 mm from the fixed end. The piezoelectric transducer has length 15 mm, width 19.05 mm, and thickness 1.4 mm. It has the following material properties: Young's moduli $E_{11} = 86$ GPa and $E_{33} = 73$ GPa, density $\rho = 9500\text{kg/m}^3$, piezoelectric constant $-1.0288 \times 10^9 \text{Vm}^{-1}$, and dielectric constant $\beta_{33} = 1.3832 \times 10^8 \text{mF}^{-1}$. The plate is discretized with 3D 20-node solid element with 12,500 elements in total. To facilitate damage identification, it is divided into 25 segments along the length direction, each with a damage index α_i. In experiment, a small resistor R (100Ω) is connected in serial to the piezoelectric transducer to measure the voltage drop across it (Fig. 6), and the current in the circuit can be obtained which then yields the admittance information. A signal analyzer (Agilent 35670A) with a source channel and the sweep sine capability is employed. The source channel is used to generate the sinusoidal voltage V_{in} sent to the piezoelectric transducer, and the output voltage V_{out} across the resistor is recorded. Without loss of generality, piezoelectric admittances and their changes upon damage occurrence are measured around the 14th (1893.58 Hz) and the 21st (3704.05 Hz) natural frequencies. 100 measurements are collected in the frequency range from 1891.69 to 1895.47 Hz and from 3700.35 to 3707.75 Hz, respectively. Correlated finite element analysis and experimental measurements are conducted so the model matches with the experimental setup in terms of admittance measurements under the healthy state.

It is worth noting that piezoelectric transducer has very high bandwidth. As such, the piezoelectric admittance can be accurately extracted at much higher frequencies than the usual vibration-based approaches. For example, in the case studies, we are able to extract admittances at the abovementioned frequency ranges. The high-frequency responses are capable of reflecting structural property changes with small characteristic sizes (i.e., small damage). As a tradeoff, a single piezoelectric admittance technique usually covers smaller structure/component for damage identification. This is generally not a problem for structures in aerospace, marine, and some infrastructure components such as wind energy components as multiple transducers can be used. The admittance value versus frequency relation is obtained based on frequency sweeping. The piezoelectric admittances are essentially harmonic responses. In our experiment, at each frequency point, 50 repeated cycles of responses are

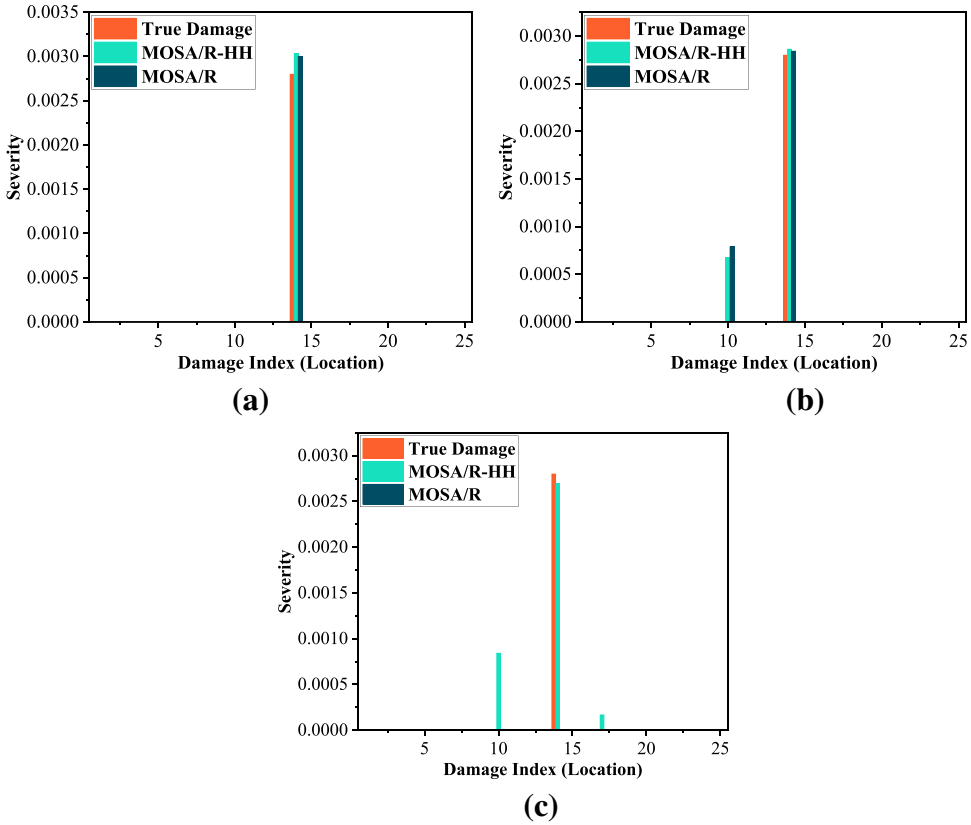

Fig. 7 Damage identification results for Case 1; 3 distinct solutions from MOSA/R-HH and 2 distinct solutions from MOSA/R

Table 4 Objective function values for case studies

Algorithms	Case 1		Case 2		Case 3	
	Obj 1	Obj 2	Obj 1	Obj 2	Obj 1	Obj 2
MOSA/R-HH	2.460×10^{-9}	1	8.361×10^{-11}	1	3.6361×10^{-5}	1
	2.36686×10^{-9}	2	8.197×10^{-11}	2	4.2474×10^{-7}	2
	2.36683×10^{-9}	3	8.111×10^{-11}	3	7.1758×10^{-8}	3
MOSA/R	2.460×10^{-9}	1	8.498×10^{-11}	1	3.6361×10^{-5}	1
	2.364×10^{-9}	2	8.212×10^{-11}	2	4.3089×10^{-7}	2
	-	-	8.172×10^{-11}	3	4.0033×10^{-7}	3

Table 5 Hypervolume index for two case studies

Algorithms	Hypervolume Index		
	Case 1	Case 2	Case 3
MOSA/R-HH	0.9	0.87	0.89
MOSA/R	0.84	0.81	0.88

recorded and then averaged. This can effectively reduce the noise effect. The admittance change before and after damage occurrence is used as input. The subtraction of the admittances before and after damage occurrence can remove possible DC shift in experiment.

In order to minimize unwanted uncertainties and variations in the experimental testbed, we use an added mass (attached to the host structure using small amount of wax) to emulate damage. Using this method, we can easily add/remove damage without altering the testbed boundary condition. The added mass causes the shift of admittance curves, which is equivalent to stiffness reduction. In our experiment, after we introduce the added mass, we extract admittance curve in the frequency range of interest. We then adjust, in the numerical model, the stiffness (i.e., reducing the Young's modulus of the elements) in the specific segment to which the mass is added, such that the admittance curve calculated matches with the experimental one (with added mass). The

percentage of stiffness reduction in the damaged segment can then be obtained numerically.

5.4 Optimization solutions and discussion

Three cases are studied here using the experimental setup and procedure outline in the preceding subsection. In the first case, we introduce damage to the 14th segment with local equivalent segment stiffness reduction 0.28%. To demonstrate and evaluate the reinforcement learning hyper-heuristic and the resulting MOSA/R-HH, we apply both MOSA/R-HH and MOSA/R (Sect. 3.1) into the case investigation.

It is worth noting that the true Pareto front for practical engineering analysis generally cannot be obtained a priori. To facilitate the computation, the term $HV\left(PF_{true}\right)$ in Eq. (2) needs to be evaluated. We take the followings steps: a) The two objectives are normalized, so the objective values are in the range of [0,1]; b) For Obj 1 in the Pareto front, we use 'linspace' in MATLAB to generate a linearly spaced vector in the range of [0,1]. Here, in this research, the number of solutions in Pareto front is set as 900, so we use 30 (square root of 900) points in the linearly generated vector; c) For Obj 2 in the Pareto front, we use $pf(2,:) = 1 - sqrt(pf(1,:))$; d) We then calculate the hypervolume using the estimated Pareto front with reference points. Here, the reference points are set as 1.1 times the boundary points of each objective; and e) The initial hypervolume of the estimated Pareto front for the damage identification case is 0.76. Note that this value can be different when different strategy is used to generate the estimated Pareto front.

In both algorithms, the maximum iterations are 100,000, the population is 150, and the number of Pareto optimal set is 9,000. The computation terminates when the maximum iteration is reached. Within 9,000 results, there are many repeated solutions after optimization convergence. After post-processing by removing the repeated ones, we obtain three distinct solutions from MOSA/R-HH and two distinct solutions from MOSA/R, shown in Fig. 7. In Fig. 7, the horizontal axis indicates the damage location, and the vertical axis indicates the severity of damage at the segment identified. The corresponding objective function values are listed in Table 4. In the table, the multiple solutions identified are arranged based on the number of non-zero entries, i.e., the second objective function in optimization. The HV values are listed in Table 5. An immediate observation from these results indicates 1) the true damage scenario is essentially included in the solution sets identified by both methods (Fig. 7(a) being the closest); and 2) MOSA/R-HH yields

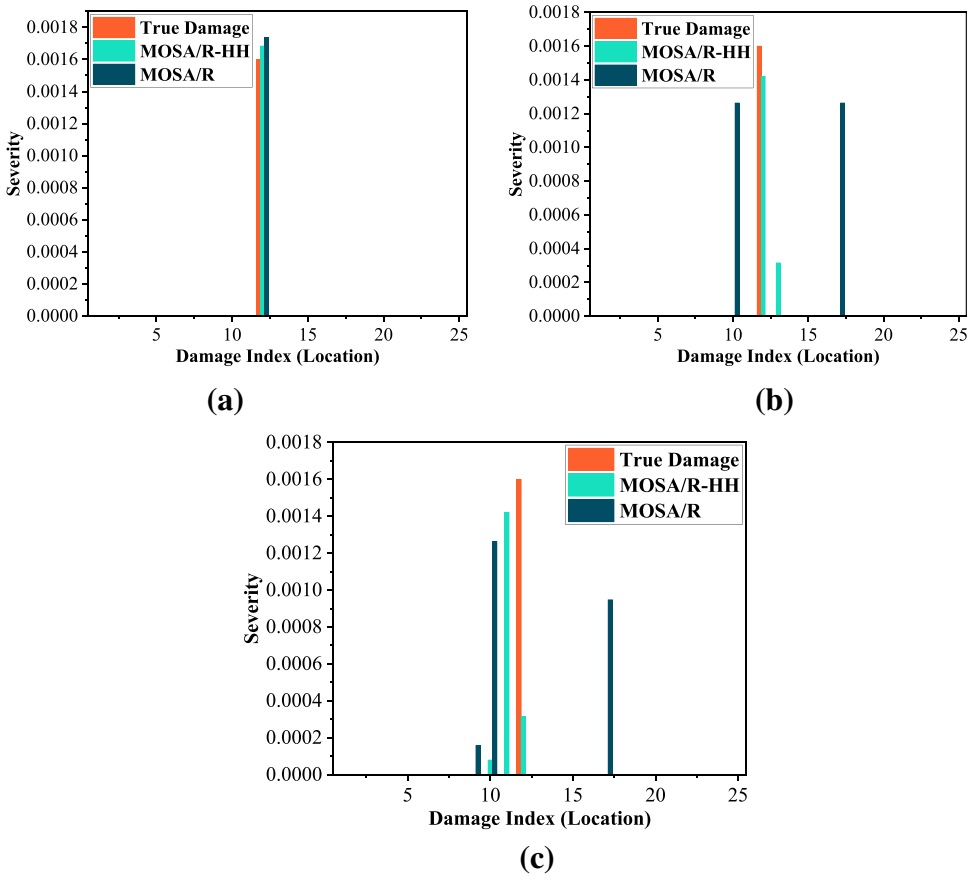

Fig. 8 Damage identification results for Case 2; 3 distinct solutions from MOSA/R-HH and 3 distinct solutions from MOSA/R

higher HV values and therefore better diversity. With the higher solution diversity and the solutions distribution, an operator will have higher confidence in making the decision.

We now further analyze the individual solutions identified. Observing Fig. 7, we can conclude that the two algorithms perform similarly in the two solutions that they both identify. In the first solution, both algorithms correctly identify the damage location (the 14th segment) and severity (~0.28%). In the second solution, in addition to the 14th segment identified, both algorithms point to the 10th segment having ~0.07% stiffness reduction. While this represents a solution that is different from the true damage scenario, it is a valid solution provided by the multi-objective optimization formulation. In this solution, the damage severity identified in the 10th segment is quite small (0.07%) as compared to the true damage severity of 0.28% at the 14th segment. Apparently, both solvers are able to find a second solution which is similar to the true damage scenario. The MOSA/R-HH further points to a third damage scenario in which the 14th segment, the 10th segment, and the 17th segment all have stiffness reductions. Nevertheless, since the 17th segment has even smaller damage severity, i.e., ~0.01%, this scenario is quite similar to the second scenario since the damage effect in the 17th segment is in the order of magnitude smaller. In general, for this first case, both MOSA/R and MOSA/R-HH can produce good results to damage identification, and the multiple solutions generated all point to the true damage scenario. The HV values listed in Table 5 confirm that MOSA/R-HH yields higher HV values and therefore better diversity. This validates the algorithm improvement.

In the second case, we introduce a smaller damage, 0.16% stiffness reduction, to the 12th segment. In damage identification, smaller size damage is generally more challenging to identify. Once again we apply both MOSA/R and MOSA/R-HH. The same set of computational parameters in the first case are employed. This time, both algorithms produce three distinct solutions as plotted in Fig. 8. These solutions are arranged in the order of non-zero entries. In the first solution, both algorithms point to the true damage scenario, i.e., ~0.16% damage in the 12th segment. It is worth noting that MOSA/R and MOSA/R-HH point to considerably different results afterward. For the second solution, MOSA/R-HH indicates damage in the 12th segment (0.14%) and the 13th segment (~0.03%). In this solution, the damage effect in the 13th segment is quite small compared to true damage severity of 0.16%, and thus this solution is close to the true damage scenario. On the other hand, MOSA/R indicates damage in the 10th segment (0.12%) and the 17th segment (0.12%). This is quite different to the true damage scenario. Similar observations can be obtained for the third solution

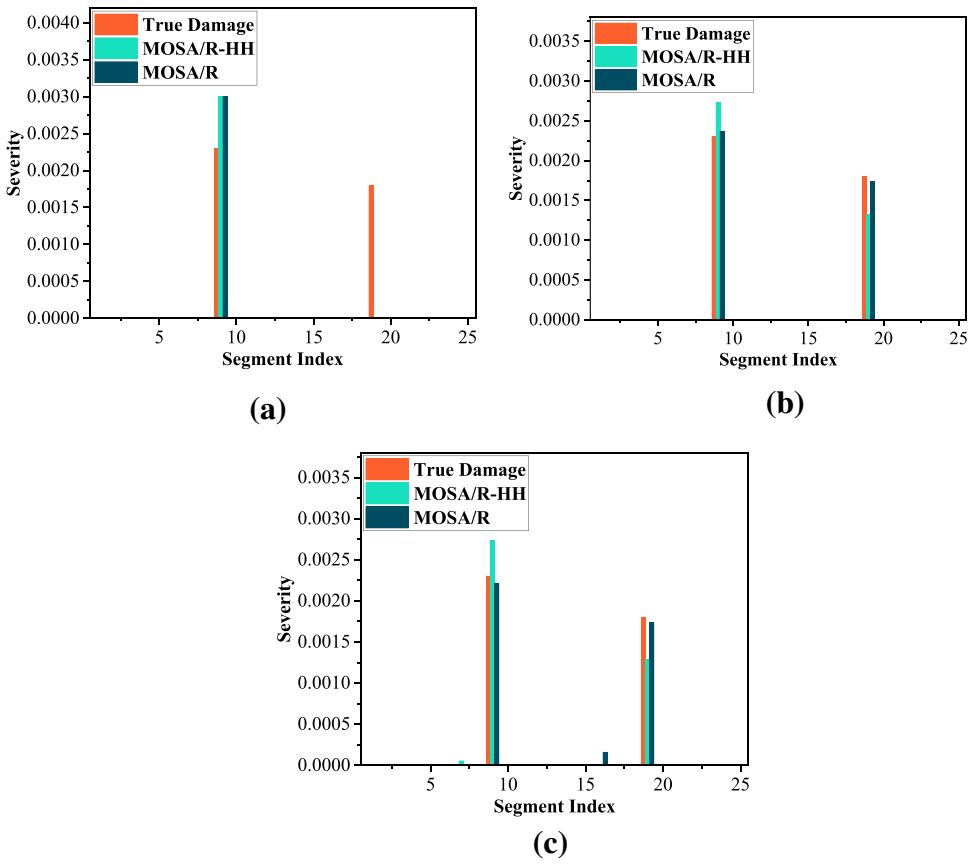

Fig. 9 Damage identification results for Case 3; 3 distinct solutions from MOSA/R-HH and 3 distinct solutions from MOSA/R

results. MOSA/R-HH indicates damage in the 11th segment (~0.14%), the 12th segment (0.03%), and the 10th segment (0.01%). Although this is different from the true damage scenario (i.e., the 12thsegment having 0.16% damage), this result is quite close from physics standpoint because the 11th segment is directly net to the 12th segment. When we examine the third solution of MOSA/R, the result is damage occurring in the 10th segment (0.13%), the 17th segment (0.09%), and the 9th segment (0.02%). This is very different from the true damage scenario. The HV values of Case 2 are reported in Table 4. As expected, MOSA/R-HH yields higher HV values and therefore better solution diversity. We can again conclude that MOSA/R-HH produces better damage identification results as all three solutions are close to the true damage scenarios. MOSA/R on the other hand produces two solutions that are quite different from the true damage scenario.

In the third case, we introduce damage to two separate locations at the 9th and the 19th segments with 0.23% and 0.18% stiffness reductions, respectively. For this multi-damage case, three solutions are produced by both algorithms, as shown in Fig. 9. The three solutions identify one, two, and three damage locations, respectively, since the second optimization objective is to minimize the number of damage locations. Consequently, both algorithms point to a single damage solution as shown in Fig. 9(a). While this solution does not match with the true damage scenario, it is not a surprise because both algorithms attempt to find optimal solutions that minimize the objective functions, and numerically they identify the single damage as an optimal solution. Meanwhile, in this solution, both algorithms are able to find one damage location correctly with close to actual severity. For solution 2 shown in Fig. 9(b), both algorithms identify the true damage locations, and the severities are fairly close to the actual values. For the third solution, both algorithms correctly identify the main damage locations and the severities obtained are close, while they both additionally point to a third damage location. MOSA/R-HH identifies a third damage at segment 7 with severity of 0.005%, and MOSA/R identifies is located at segment 17 with severity of 0.016%. These two severity values are very small as compared to those of the main damage locations. Thus, the third solution identified by both algorithms is similar to the second solution, and both solutions point to the true damage scenario with good accuracy. The results obtained in this case demonstrate the ability of the proposed algorithm to handle the multiple damage case. It is worth noting that the damage identification cases are all conducted using experimental data which inevitably is subject to noise and various uncertainties. The results obtained by MOSA/R-HH demonstrate its capability of producing damage identification results in an accurate and robust manner.

6 Conclusions

In this research, we formulate an autonomous hyper-heuristic scheme that works coherently with multi-objective simulated annealing, featuring domination amount, crowding distance, and hypervolume calculations. The hyper-heuristic scheme can be adjusted at a high level by changing heuristic selection and credit assignment strategies or at a low level by customizing the heuristic repository to meet different optimization requirements. It can also be used to investigate the relation between heuristics and problem instances. The proposed MOSA/R-HH is shown to yield better results than other MOSA algorithms like AMOSA and representative evolutionary algorithms like NSGA-II and MOEA/D in benchmark test cases. The proposed hyper-heuristic approach is then applied to piezoelectric admittance-based active interrogation for structural health monitoring. By comparing with MOSA/R without hyper-heuristic, we successfully demonstrate that the new algorithm can identify damage scenario with enhanced accuracy and robustness.

Acknowledgements This research is supported in part by a Space Technology Research Institutes Grant (No. 80NSSC19K1076) from NASA's Space Technology Research Grants Program and in part by NSF under Grant CMMI-1825324.

Declarations

Conflict of interest On behalf of all authors, the corresponding author states that there is no conflict of interest.

Replication of results All the algorithms and analyses are implemented through MATLAB. All related data including simulation data and experimental data are available from the corresponding author upon request.

References

Antunes CH, Lima P, Oliveira E, Pires DF (2011) A multi-objective simulated annealing approach to reactive power compensation. Eng Optim 43(10):1063–1077

Bai R, Blazewicz J, Burke EK, Kendall G, McCollum B (2012) A simulated annealing hyper-heuristic methodology for flexible decision support. 4OR 10(1):43–66

Bandyopadhyay S, Saha S, Maulik U, Deb K (2008) A simulated annealing-based multiobjective optimization algorithm: AMOSA. IEEE Trans Evol Comput 12(3):269–283

Burke EK, Hyde MR, Kendall G, Ochoa G, Ozcan E, Woodward JR (2009) Exploring hyper-heuristic methodologies with genetic programming. Computational intelligence. Springer, Berlin, pp 177–201

Burke EK, Gendreau M, Hyde M, Kendall G, Ochoa G, Özcan E, Qu R (2013) Hyper-heuristics: A survey of the state of the art. Journal of the Operational Research Society 64(12):1695–1724

Cao P, Shuai Q, Tang J (2018a) A multi-objective DIRECT algorithm toward structural damage identification with limited dynamic

response information. J Nondestruct Evaluat Diagn Progn Eng Syst 1(2):021004
Cao P, Qi S, Tang J (2018b) Structural damage identification using piezoelectric impedance measurement with sparse inverse analysis. Smart Mater Struct 27(3):035020
Cao P, Fan Z, Gao RX, Tang J (2019) Harnessing multi-objective simulated annealing toward configuration optimization within compact space for additive manufacturing. Robot Comput Integr Manuf 57:29–45
Cowling P, Kendall G, Soubeiga E (2000) A hyperheuristic approach to scheduling a sales summit. International Conference on the Practice and Theory of Automated Timetabling. Springer, Berlin, pp 176–190
Cha YJ, Buyukozturk O (2015) Structural damage detection using modal strain energy and hybrid multiobjective optimization. Comput Aid Civ Infrastruct Eng 30(5):347–358
Deb K, Thiele L, Laumanns M, Zitzler E (2002a) Scalable multi-objective optimization test problems. Congress on Evolutionary Computation. IEEE Press, pp 825–830
Deb K, Pratap A, Agarwal S, Meyarivan TAMT (2002b) A fast and elitist multiobjective genetic algorithm: NSGA-II. IEEE Trans Evol Comput 6(2):182–197
Deb K, Agrawal S, Pratap A, Meyarivan T (2000) A fast elitist non-dominated sorting genetic algorithm for multi-objective optimization: NSGA-II. International conference on parallel problem solving from nature. Springer, Berlin, pp 849–858
Dinh-Cong D, Nguyen-Thoi T (2021) An effective damage identification procedure using model updating technique and multi-objective optimization algorithm for structures made of functionally graded materials. Engineering with Computers, in press.
Emmerich M, Beume N, Naujoks, B (2005) An EMO algorithm using the hypervolume measure as selection criterion. In: International Conference on Evolutionary Multi-Criterion Optimization, pp 62–76. Springer, Berlin
Guizzo G, Fritsche GM, Vergilio SR, Pozo ATR (2015) A hyper-heuristic for the multi-objective integration and test order problem. In Proceedings of the 2015 Annual Conference on Genetic and Evolutionary Computation, pp 1343–1350. ACM
Goldberg DE (1990) Probability matching, the magnitude of reinforcement, and classifier system bidding. Mach Learn 5(4):407–425
Gomes GF, Mendéz YAD, da Cunha SS, Ancelotti AC (2018) A numerical–experimental study for structural damage detection in CFRP plates using remote vibration measurements. J Civ Struct Heal Monit 8(1):33–47
Hitomi N, Selva D (2015) The effect of credit definition and aggregation strategies on multi-objective hyper-heuristics. In: ASME 2015 International Design Engineering Technical Conferences and Computers and Information in Engineering Conference (pp: V02BT03A030-V02BT03A030). American Society of Mechanical Engineers
Hitomi N, Selva D (2016) A classification and comparison of credit assignment strategies in multiobjective adaptive operator selection. IEEE Trans Evol Comput 21(2):294–314
Ishibuchi H, Sakane Y, Tsukamoto N, Nojima Y (2010) Simultaneous use of different scalarizing functions in MOEA/D. In: Proceedings of the 12th annual conference on Genetic and evolutionary computation, pp 519–526. ACM
Ishibuchi H, Masuda H, Tanigaki Y, Nojima Y (2015) Modified distance calculation in generational distance and inverted generational distance. In International conference on evolutionary multi-criterion optimization, pp 110–125. Springer, Cham
Kaveh A, Laknejadi K (2013) A new multi-swarm multi-objective optimization method for structural design. Adv Eng Softw 58:54–69
Kirkpatrick S, Gelatt CD, Vecchi MP (1983) Optimization by simulated annealing. Science, New Series 220(4598):671–680
Krempser E, Fialho Á, Barbosa HJ (2012) Adaptive operator selection at the hyper-level. In: International Conference on Parallel Problem Solving from Nature, pp 378–387. Springer, Berlin
Li M, Yang S, Liu X (2016) Pareto or non-pareto: bi-criterion evolution in multiobjective optimization. IEEE Trans Evol Comput 20(5):645–665
Lu C, Xiao S, Li X, Gao L (2016) An effective multi-objective discrete grey wolf optimizer for a real-world scheduling problem in welding production. Adv Eng Softw 99:161–176
Maturana, Fialho, Á, Saubion F, Schoenauer M, Sebag M (2009) Extreme compass and dynamic multi-armed bandits for adaptive operator selection. In: 2009 IEEE Congress on Evolutionary Computation, pp 365–372. IEEE
Lipowski A, Lipowska D (2012) Roulette-wheel selection via stochastic acceptance. Physica A 391(6):2193–2196
McClymont K, Keedwell EC (2011) Markov chain hyper-heuristic (MCHH): an online selective hyper-heuristic for multi-objective continuous problems. In: Proceedings of the 13th annual conference on genetic and evolutionary computation, pp 2003–2010. ACM
Mohd Zain MZ, Kanesan J, Chuah J, Dhanapal S, Kendall G (2018) A multi-objective particle swarm optimization algorithm based on dynamic boundary search for constrained optimization. Appl Soft Comput 70:680–700
Maashi M, Kendall G, Özcan E (2015) Choice function based hyper-heuristics for multi-objective optimization. Appl Soft Comput 28:312–326
Nareyek A (2003) Choosing search heuristics by non-stationary reinforcement learning. Metaheuristics: Computer decision-making. Springer, Boston, pp 523–544
Özcan E, Misir M, Ochoa G, Burke EK (2012) A reinforcement learning: great-deluge hyper-heuristic for examination timetabling. Modeling, analysis, and applications in metaheuristic computing: advancements and trends. IGI Global
Qin W, Zhuang Z, Huang Z, Huang H (2021) A novel reinforcement learning-based hyper-heuristic for heterogeneous vehicle routing problem. Comput Ind Eng 156:107252
Shuai Q, Zhou K, Zhou S, Tang J (2017) Fault identification using piezoelectric impedance measurement and model-based intelligent inference with pre-screening. Smart Mater Struct 26(4):045007
Suman B (2004) Study of simulated annealing based algorithms for multiobjective optimization of a constrained problem. Comput Chem Eng 28(9):1849–1871
Suman B, Kumar P (2006) A survey of simulated annealing as a tool for single and multiobjective optimization. J Oper Res Soc 57(10):1143–1160
Smith KI (2006) A study of simulated annealing techniques for multi-objective optimisation. University of Exeter, Thesis
Szőllős A, Šmíd M, Hájek J (2009) Aerodynamic optimization via multi-objective micro-genetic algorithm with range adaptation, knowledge-based reinitialization, crowding and ε-dominance. Adv Eng Softw 40(6):419–430
Thierens D (2007) Adaptive strategies for operator allocation. Parameter Setting in Evolutionary Algorithms. Springer, Berlin, pp 77–90
Tiachacht S, Bouazzouni A, Khatir S, Wahab MA, Behtani A, Capozucca R (2018) Damage assessment in structures using combination of a modified Cornwell indicator and genetic algorithm. Eng Struct 177:421–430
Wang KW, Tang J (2008) Adaptive Structural System with Piezoelectric Transducer Circuitry. Springer
Wang WX, Wang X, Ge XL, Deng L (2014) Multi-objective optimization model for multi-project scheduling on critical chain. Adv Eng Softw 68:33–39
Ye HL, Zhang Y, Yang QS, Xiao YN, Grandhi RV, Fischer CC (2017) Optimal design of a three tape-spring hinge deployable space

structure using an experimentally validated physics-based model. Struct Multidisc Optim 56(5):973–989

Ye HL, Zhang Y, Yang QS, Zhang B (2019) Quasi-static analysis and multi-objective optimization for tape spring hinge. Struct Multidisc Optim 60(6):2417–2430

Zavala GR, Nebro AJ, Luna F, Coello CAC (2014) A survey of multi-objective metaheuristics applied to structural optimization. Struct Multidisc Optim 49(4):537–558

Zavala G, Nebro AJ, Luna F, Coello CAC (2016) Structural design using multi-objective metaheuristics. Comparative study and application to a real-world problem. Struct Multidisc Optim 53(3):545–566

Zhang Q, Li H (2007) MOEA/D: a multiobjective evolutionary algorithm based on decomposition. IEEE Trans Evol Comput 11(6):712–731

Zhang Q, Zhou A, Zhao S, Suganthan PN, Liu W, Tiwari S (2008) Multiobjective optimization test instances for the CEC 2009 special session and competition. University of Essex, Colchester, UK and Nanyang technological University, Singapore, special session on performance assessment of multi-objective optimization algorithms, technical report, 264

Zitzler E, Thiele L (1999) Multiobjective evolutionary algorithms: A comparative case study and the strength Pareto approach. IEEE Trans Evol Comput 3(4):257–271

Zitzler E, Brockhoff D, Thiele L (2007) The hypervolume indicator revisited: On the design of Pareto-compliant indicators via weighted integration. International Conference on Evolutionary Multi-Criterion Optimization. Springer, Berlin, pp 862–876

Zhou A, Qu BY, Li H, Zhao SZ, Suganthan PN, Zhang Q (2011) Multiobjective evolutionary algorithms: a survey of the state of the art. Swarm Evol Comput 1(1):32–49

Zarchi M, Attaran B (2019) Improved design of an active landing gear for a passenger aircraft using multi-objective optimization technique. Struct Multidisc Optim 59(5):1813–1833

Zhang S, Ren Z, Li C, Xuan J (2020) A perturbation adaptive pursuit strategy based hyper-heuristic for multi-objective optimization problems. Swarm Evol Comput 54:100647